



AIAA 98–2443

**Diffusion Characteristics of Upwind
Schemes on Unstructured
Triangulations**

William A. Wood and William L. Kleb

NASA Langley Research Center, Hampton, VA 23681

29th AIAA Fluid Dynamics Conference
June 15–18, 1998/Albuquerque, NM

Diffusion Characteristics of Upwind Schemes on Unstructured Triangulations

William A. Wood* and William L. Kleb*

NASA Langley Research Center, Hampton, VA 23681

The diffusive characteristics of two upwind schemes, multi-dimensional fluctuation splitting and dimensionally-split finite volume, are compared for scalar advection-diffusion problems. Algorithms for the two schemes are developed for node-based data representation on median-dual meshes associated with unstructured triangulations in two spatial dimensions. Four model equations are considered: linear advection, non-linear advection, diffusion, and advection-diffusion. Modular coding is employed to isolate the effects of the two approaches for upwind flux evaluation, allowing for head-to-head accuracy and efficiency comparisons. Both the stability of compressive limiters and the amount of artificial diffusion generated by the schemes is found to be grid-orientation dependent, with the fluctuation splitting scheme producing less artificial diffusion than the dimensionally-split finite volume scheme. Convergence rates are compared for the combined advection-diffusion problem, with a speedup of 2–3 seen for fluctuation splitting versus finite volume when solved on the same mesh. However, accurate solutions to problems with small diffusion coefficients can be achieved on coarser meshes using fluctuation splitting rather than finite volume, so that when comparing convergence rates to reach a given accuracy, fluctuation splitting shows a 20–25 speedup over finite volume.

Nomenclature

A, B	Flux Jacobians	ξ, η	Curvilinear coordinates
c	Nodal update coefficients	τ	Timestep
\vec{F}	Convective flux vector, $\vec{F} = \vec{F}(x, y, u)$	Φ	Artificial dissipation—finite volume
h	Mesh spacing	ϕ	Element advective fluctuation
\hat{i}, \hat{j}	Cartesian unit vectors	ϕ^ξ, ϕ^η	Fluctuation components
J^{-1}	Inverse Jacobian of the coordinate transformation	$\phi^{\xi*}, \phi^{\eta*}$	Limited fluctuations
ℓ	Edge length	$\bar{\phi}^\xi, \bar{\phi}^\eta$	Artificial dissipation—fluctuation splitting
\hat{n}	Outward unit normal to control cell	ϕ_v	Viscous fluctuation
\mathbf{n}	Length-scaled inward normal	ψ	Limiter function
Q	Fluctuation ratio	Ω	Area of control cell
\vec{r}	Distance vector from node to face	∇	Gradient operator
S_i	Median-dual area about node i		
t	Time		
u	Dependent variable		
x, y	Cartesian coordinates		
α, β	Curvilinear advection speeds		
γ	Boundary of control cell		
γ	Limiter bound		
ϑ	Finite element linear shape function		
$\vec{\lambda}$	Advection velocity vector		
ν	Diffusion coefficient		

Introduction

UPWIND discretizations for advection equations typically introduce artificial numerical dissipation into the solution. When combined advection-diffusion problems are considered, this dissipation introduced in the discretization of the advection terms should be less than the true physical diffusion. To this end the diffusive characteristics of upwind schemes are investigated and their performance in resolving solutions to advection-diffusion problems with small diffusion coefficients is analyzed.

Two node-based, median-dual methods for modeling convective fluxes are considered. The first is a traditional dimensionally-split finite volume (FV) scheme.¹ Dimensionally-split schemes are known to introduce excess dissipation when discontinuities are not aligned with the mesh.²

The second method is the NNL³ fluctuation splitting

*Aerospace Engineer, Aerothermodynamics Branch, Aero- and Gas-Dynamics Division.

Copyright © 1998 by the American Institute of Aeronautics and Astronautics, Inc. No copyright is asserted in the United States under Title 17, U.S. Code. The U.S. Government has a royalty-free license to exercise all rights under the copyright claimed herein for Governmental Purposes. All other rights are reserved by the copyright owner.

(FS) scheme. FS has a more-compact stencil than FV for second-order formulations and exhibits “zero cross-diffusion”[†] in a grid-aligned condition. Both of these attributes should lead to less introduced dissipation as compared with FV. The sensitivity of FS to grid orientation and resulting production of cross-diffusion is investigated in the present report.

The use of compressive limiter functions is investigated with both algorithms. Also, local timesteps based on positivity arguments are tested, and in some cases the optimum timestep for convergence is found to be less than the largest stable timestep. This behavior is attributed to residual oscillations forced by “ringing” of the limiter functions.

Formulation of FS schemes for diffusion problems is a recent research area.^{4,5} The present study seeks to quantify the relative merits of using a low-diffusion advection operator to resolve advection-diffusion problems with small diffusion coefficients. Lessons learned on these problems will guide the development of computer codes for solving compressible viscous fluid dynamic problems.

Governing Equations

The non-linear advection/diffusion equation,

$$u_t + \nabla \cdot \vec{F} = \nabla \cdot (\nu \nabla u) \quad (1)$$

is cast as a hyperbolic conservation law, to which steady-state solutions are sought.

Finite Volume

In FV form, using the divergence theorem Eqn. 1 becomes,

$$\int_{\Omega} u_t d\Omega = - \oint_{\partial \Omega} (\vec{F} - \nu \nabla u) \cdot \hat{n} d, \quad (2)$$

where Ω is the median dual about node i and $\partial \Omega$ is the boundary of Ω . Using mass lumping to the nodes, similar to an explicit finite element treatment,⁶ the temporal evolution is evaluated on a time-invariant mesh as,

$$\int_{\Omega} u_t d\Omega = S_i \frac{\partial u_i}{\partial t} \rightarrow \frac{S_i}{\tau} (u_i^{t+\tau} - u_i^t) \quad (3)$$

The discretization of the convective flux, \vec{F} , is performed using Barth’s implementation¹ of the upwind, locally one-dimensional, approximate Riemann problem of Roe.⁷

$$\oint_{\partial \Omega} \vec{F} \cdot \hat{n} d, \rightarrow \sum_{\text{faces}} \left[\frac{1}{2} (\vec{F}_{in} + \vec{F}_{out}) \cdot \hat{n} - \Phi \right] \Delta, \quad (4)$$

[†] “Zero cross diffusion” refers to the practice of adding artificial diffusion terms in the streamwise direction only, as opposed to adding artificial dissipation in both the streamwise and cross-stream directions.

where the artificial dissipation provides the upwinding,

$$\Phi = \frac{1}{2} |\tilde{A} \hat{n}_x + \tilde{B} \hat{n}_y| (u_{out} - u_{in}) \quad (5)$$

with $\hat{n} = \hat{n}_x \hat{i} + \hat{n}_y \hat{j}$. *Out* and *in* refer to states on the outside and inside of Ω at the face. A and B are the flux Jacobians,

$$A = \frac{\partial F^{(1)}}{\partial u}, \quad B = \frac{\partial F^{(2)}}{\partial u} \quad (6)$$

and (\tilde{A}, \tilde{B}) represent their conservative linearizations at the cell face.⁷

Reconstruction from the nodal unknowns to the cell faces, as,

$$u_{face} = u_i + \psi \nabla u \cdot \vec{r} \quad (7)$$

is performed with Barth’s limited, unweighted least-squares procedure to provide second-order spatial accuracy in smoothly-varying regions of the solution.

Two methods for evaluating the diffusion term are incorporated into FV. The more compact of the two, the finite element discretization, is discussed in the following section. The less-compact diffusion formula is obtained by discretizing the last term of Eqn. 2, in a manner similar to Eqn. 4,

$$\oint_{\partial \Omega} \nu \nabla u \cdot \hat{n} d, \rightarrow \sum_{\text{faces}} \frac{\bar{\nu}}{2} (\nabla u_{in} + \nabla u_{out}) \cdot \hat{n} \Delta, \quad (8)$$

The diffusion coefficient is averaged over the length of the face. The gradients from Eqn. 7 are not limited before averaging at the control-volume faces in Eqn. 8, as suggested by Anderson and Bonhaus.⁸

Fluctuation Splitting

The NNL FS scheme is presented as a slight re-interpretation of the work of Sidilkover and Roe.³ The current interpretation is as a volume integral over triangular elements, without recourse to the divergence theorem. The discretized equations, however, are identical.

Integrating Eqn. 1 over an element, where Ω is now the area of the triangular element,

$$\int_{\Omega} u_t d\Omega = - \int_{\Omega} \nabla \cdot \vec{F} d\Omega + \int_{\Omega} \nabla \cdot (\nu \nabla u) d\Omega \quad (9)$$

For linear variation of the dependent variable over the element, the temporal evolution is,

$$\int_{\Omega} u_t d\Omega = \Omega \bar{u}_t = \frac{\Omega}{3} (u_{1_t} + u_{2_t} + u_{3_t}) \quad (10)$$

where u_1 , u_2 , and u_3 correspond to the three nodes defining element Ω .

Defining local curvilinear coordinates, ξ and η , parallel to sides $\bar{12}$ and $\bar{23}$, respectively (Fig. 1), the divergence of the convective flux can be written,

$$\nabla \cdot \vec{F} = F_x^{(1)} + F_y^{(2)} = \frac{1}{J-1} (\hat{n}_2 \cdot \vec{F}_{\xi} - \hat{n}_1 \cdot \vec{F}_{\eta}) \quad (11)$$

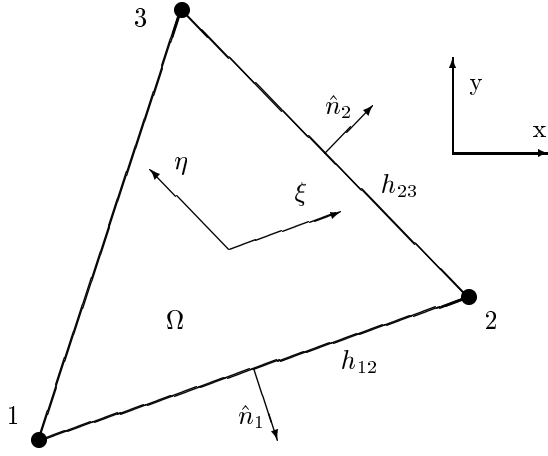


Fig. 1 Fluctuation splitting element nomenclature.

Defining the scaled inward normal, $\mathbf{n} = -h\hat{n}$, where h is a mesh edge length, the divergence (Eqn. 11) becomes,

$$\nabla \cdot \vec{F} = \frac{1}{2\Omega} \left(-h_{12}\mathbf{n}_2 \cdot \vec{F}_\xi + h_{23}\mathbf{n}_1 \cdot \vec{F}_\eta \right) \quad (12)$$

If \vec{F} is linear or quadratic in u , then for a linear variation of u over the element,

$$\int_{\Omega} \nabla \cdot \vec{F} d\Omega = \alpha \Delta_{21}u + \beta \Delta_{32}u \quad (13)$$

where the difference operator is defined $\Delta_{21}u = u_2 - u_1$ and the advection speeds are,

$$\alpha = -\frac{1}{2}(\mathbf{n}_{2x}\tilde{A} + \mathbf{n}_{2y}\tilde{B}), \quad \beta = \frac{1}{2}(\mathbf{n}_{1x}\tilde{A} + \mathbf{n}_{1y}\tilde{B}) \quad (14)$$

\tilde{A} and \tilde{B} are now the conservative linearizations over the triangular element.⁹

The advective fluctuation can be defined,

$$\phi = - \int_{\Omega} \nabla \cdot \vec{F} d\Omega \quad (15)$$

The fluctuation can be split,

$$\phi = \phi^\xi + \phi^\eta \quad (16)$$

where,

$$\phi^\xi = -\alpha \Delta_{21}u, \quad \phi^\eta = -\beta \Delta_{32}u \quad (17)$$

Following Sidilkover¹⁰ the fluctuation is limited to achieve a second-order scheme,

$$\phi^{\xi*} = \phi^\xi + \phi^\eta \psi(Q) = \phi^\xi \left(1 - \frac{\psi(Q)}{Q} \right) \quad (18)$$

$$\phi^{\eta*} = \phi^\eta - \phi^\eta \psi(Q) = \phi^\eta (1 - \psi(Q)) \quad (19)$$

with,

$$Q = -\frac{\phi^\xi}{\phi^\eta} \quad (20)$$

Upwinding is achieved through the introduction of the artificial dissipation terms,

$$\bar{\phi}^\xi = \text{sign}(\alpha)\phi^{\xi*}, \quad \bar{\phi}^\eta = \text{sign}(\beta)\phi^{\eta*} \quad (21)$$

Combining Eqn. 10 with a distribution scheme for Eqn. 15 and summing over all elements, the contributions to nodal time derivatives can be written in the form,

$$\begin{aligned} S_1 u_{1t} &\leftarrow \frac{1}{2}(\phi^{\xi*} - \bar{\phi}^\xi) + COE \\ S_2 u_{2t} &\leftarrow \frac{1}{2}(\phi^{\xi*} + \bar{\phi}^\xi) + \frac{1}{2}(\phi^{\eta*} - \bar{\phi}^\eta) + COE \\ S_3 u_{3t} &\leftarrow \frac{1}{2}(\phi^{\eta*} + \bar{\phi}^\eta) + COE \end{aligned} \quad (22)$$

where COE stands for contributions from other elements containing these nodes.

A finite element treatment, similar to Tomaich,⁴ is employed to obtain the diffusive fluctuation,

$$\phi_v = \int_{\Omega} \nabla \cdot (\nu \nabla u) d\Omega \quad (23)$$

Assuming piecewise-linear data and an element-averaged diffusion coefficient leads to a diffusive fluctuation of zero for the triangular element. Introducing the linear nodal shape functions ϑ_i , such that $\sum_{i=1}^3 \vartheta_i = 1$, the elemental diffusive fluctuation can be expressed $\phi_v = \sum_{i=1}^3 \phi_{v_i} = 0$, where

$$\phi_{v_i} = \int_{\Omega} \vartheta_i \nabla \cdot (\bar{\nu} \nabla u) d\Omega \quad (24)$$

Integrating by parts,

$$\phi_{v_i} = \oint \vartheta_i \bar{\nu} \nabla u \cdot \hat{n} d, - \int_{\Omega} \bar{\nu} \nabla u \cdot \nabla \vartheta_i d\Omega \quad (25)$$

The boundary integral in Eqn. 25 will cancel on summing contributions for interior nodes. The remaining volume integral can be evaluated analytically,

$$\phi_{v_i} = -\frac{\bar{\nu}}{2} \nabla u \cdot \mathbf{n}_{i+1} = -\frac{\bar{\nu}}{4\Omega} \sum_{j=1}^3 u_j \mathbf{n}_{j+1} \cdot \mathbf{n}_{i+1} \quad (26)$$

Distributing this diffusive fluctuation to the nodes and keeping only the larger of the physical or artificial dissipation leads to the update formula,

$$\begin{aligned} S_1 u_{1t} &\leftarrow \frac{\phi^{\xi*}}{2} + \max \left(-\frac{\bar{\phi}^\xi}{2}, \phi_{v_1} \right) + COE \\ S_2 u_{2t} &\leftarrow \frac{\phi^{\xi*} + \phi^{\eta*}}{2} + \max \left(\frac{(\bar{\phi}^\xi - \bar{\phi}^\eta)}{2}, \phi_{v_2} \right) + COE \\ S_3 u_{3t} &\leftarrow \frac{\phi^{\eta*}}{2} + \max \left(\frac{\bar{\phi}^\eta}{2}, \phi_{v_3} \right) + COE \end{aligned} \quad (27)$$

Boundary Conditions

Explicit Dirichlet inflow boundary conditions are employed. Advective outflow boundaries are treated for free convection through the boundary nodes, allowing boundary nodes to be handled in the same manner as interior nodes. For the diffusion terms a Neumann outflow boundary is applied with zero gradient, achieved by setting the boundary integral in Eqn. 25 to zero.

Limiter Functions

The limiter functions employed by both schemes are cast as a limit on the ratio of two values. The limiting proposed by Barth¹ is interpreted as a non-symmetric limiter¹¹ consistent with one-dimensional limiting in the maximum gradient direction. The limiting on the reconstruction (Eqn. 7) is performed on the ratio,

$$\psi = \psi \left(\frac{u^{min/max} - u_i}{2\nabla u \cdot \vec{r}} \right) \quad (28)$$

where $u^{min/max}$ is the minimum (resp. maximum) of u_i and all distance-one neighbors. This same interpretation has been put forth by Bruner and Walters,¹² though they identified Barth's limiting with the symmetric Superbee limiter, rather than the non-symmetric Chakravarthy and Osher¹¹ limiter.

Minmod, van Albada,¹³ Superbee, and γ ¹⁴ symmetric limiters are utilized for FV (Eqn. 7) and FS (Eqns. 18 and 19). The γ limiter, of which the Minmod ($\gamma = 1$) and Superbee ($\gamma = 2$) are special cases, is,

$$\psi_\gamma(Q) = \max[0, \min(\gamma Q, 1), \min(Q, \gamma)] \quad (29)$$

Timestep

Both schemes are formulated either as Gauss-Seidel time-relaxation or forward Euler time-evolution algorithms.

The nodal updates for the discrete system can be formed as a sum of contributions from all nodes.

$$u_i^{t+\tau} = \sum_j c_j u_j = c_i u_i + \sum_{j \neq i} c_j u_j \quad (30)$$

For positivity¹⁵ each of the coefficients in Eqn. 30 must be non-negative.

Advective Timestep restriction

In the FV context the nodal update (Eqn. 30) can be rearranged into the form of Eqn. 3,

$$\frac{S_i}{\tau} (u_i^{t+\tau} - u_i^t) = \frac{S_i}{\tau} (c_i - 1) u_i + \frac{S_i}{\tau} \sum_{j \neq i} c_j u_j \quad (31)$$

For the upwind, edge-based algorithm considered here, each $\frac{S_i}{\tau} c_j$ will be related to a positive-definite coefficient equal to zero for outflowing faces and related to

the wavespeed for inflowing faces, yielding the restriction $\tau \geq 0$ on the timestep. The remaining term can be expressed,

$$\frac{S_i}{\tau} (c_i - 1) = - \sum_{k \text{ about } i} c_k \quad (32)$$

where the c_k coefficients are also positive-definite, either zero for inflowing faces or related to the wavespeed for outflowing faces. Rearranging and imposing the positivity constraint, $c_i \geq 0$, yields the timestep restriction,

$$1 - \frac{\tau}{S_i} \sum_{k \text{ about } i} c_k = c_i \geq 0 \quad (33)$$

$$\tau \leq \frac{S_i}{\sum_{k \text{ about } i} c_k} \quad (34)$$

For FS, the nodal updates are assembled from Eqn. 22 as,

$$\frac{S_i}{\tau} (u_i^{t+\tau} - u_i^t) = \sum_{j \neq i} c_j (u_j - u_i) \quad (35)$$

In this case the c_j coefficients are formed as contributions from the fluctuations in the triangles to both the left and the right of mesh edge \overline{ij} . The positivity restriction on τ is found to have a similar form as for finite volume (Eqn. 34),

$$\tau \leq \frac{S_i}{\sum_{j \neq i} c_j} \quad (36)$$

Local time-stepping based on positivity is shown to yield stable, yet non-converging, solutions in some second-order cases (see Results section). Robust convergence is obtained by using the first-order c 's in Eqns. 34 and 36, even for second-order-accurate spatial discretizations.

Diffusive Timestep Restriction

Unfortunately, the finite element formulation for the diffusive terms (Eqn. 26) cannot be guaranteed to preserve local positivity on obtuse triangles (see Barth¹). Considering only the contributions from the current node, the coefficient for the diffusion term can be written,

$$u_i^{t+\tau} = u_i^t \left(1 - \frac{\tau}{S_i} \sum_T \frac{\nu \ell^2}{4\Omega} \right) \quad (37)$$

The appropriate edge length is the side of the element opposite the current node. The resulting timestep restriction is,

$$\tau \leq \frac{S_i}{\sum_T \frac{\nu \ell^2}{4\Omega}} \quad (38)$$

In a similar manner the timestep restriction from Eqn. 8 is,

$$\tau \leq \frac{S_i}{\sum_T \frac{3\nu \Delta_i^2}{4\Omega}} \quad (39)$$

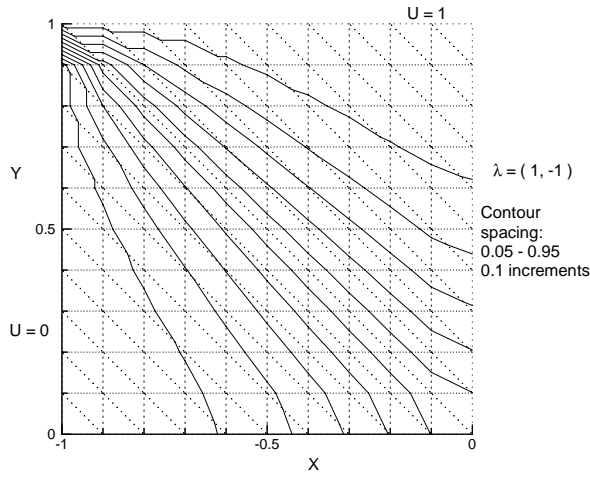


Fig. 2 First-order fluctuation splitting, uniform advection.

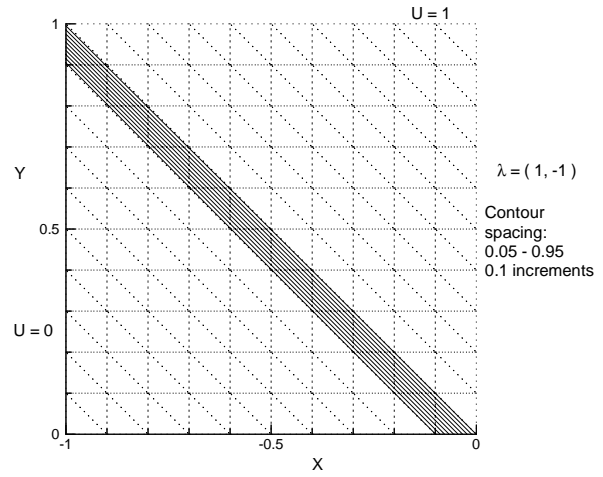


Fig. 3 Second-order fluctuation splitting, uniform advection.

Results

Linear Advection

The linear advection equation is obtained from Eqn. 1 by setting $\nu = 0$ and $\vec{F} = \vec{\lambda}u$, yielding,

$$u_t + \nabla \cdot (\vec{\lambda}u) = 0 \quad (40)$$

A divergence-less advection velocity is considered, such that $\nabla \cdot \vec{\lambda} = 0$. Equation 40 can then be written,

$$u_t + \vec{\lambda} \cdot \nabla u = 0 \quad (41)$$

Uniform Advection

Uniform advection of the Heavyside function at -45 degrees, $\vec{\lambda} = (1, -1)$, on a cut-cartesian mesh is shown for first-order FS, second-order FS, and second-order FV in Figs. 2–4, respectively. The mesh is shown as the dashed background, and equally-spaced contours vary on $[0,1]$, the minimum and maximum solution values. The spread of the contour lines with spatial evolution is indicative of the amount of dissipation introduced into the solution by the discretization of the convective terms.

Second-order FS is seen to be greatly superior to first-order, as expected, reproducing the exact solution in this case with no introduced dissipation. Also, FS represents a significant reduction in numerical diffusion versus the corresponding FV scheme, with both results employing the Minmod limiter.

However, the “zero cross-diffusion” results of Fig. 3 with FS are misleading. In Fig. 5 the advection velocity has been rotated counter clockwise by 90 degrees on the same grid. Clearly, the artificial dissipation introduced by the FS scheme has been increased.

The corresponding FV solution is shown in Fig. 6. While the change in contour spreading for the FV scheme between Figs. 4 and 6 is less dramatic than the change in spreading for the FS scheme in Figs. 3

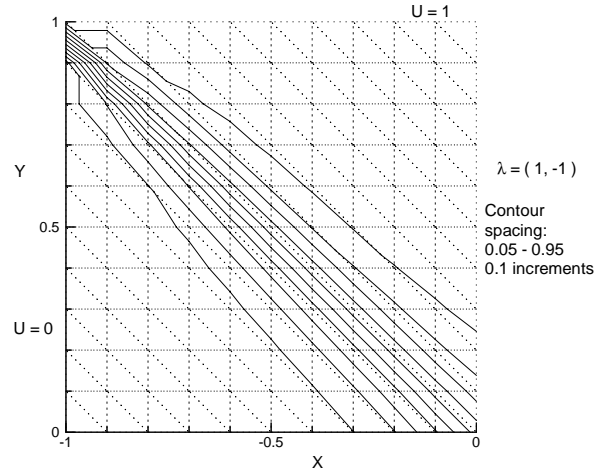


Fig. 4 Second-order finite volume, uniform advection.

and 5, the FS results still exhibit less diffusion than the FV results, comparing Figs. 5 and 6.

Employing the compressive Superbee limiter with the FS scheme yields the results of Fig. 7. In this case the discontinuity is confined to a 2–3 cell stencil, and does not grow in space. Applying the Superbee limiter to FV cannot eliminate all artificial dissipation for this case, as is possible with FS. The FV results (not shown) corresponding to Fig. 7 spread the discontinuity over four cells by the outflow boundary, with a continually broadening trend.

However, while it is possible to use the Superbee limiter with FS for this case, compressive limiters can be unstable on different grid orientations. For example, no degree of compression is stable for the case of Fig. 3. This potential for instability is related to global positivity, as discussed by Sidilkover and Roe.³

The effect of using a general unstructured grid is investigated in Figs. 8 and 9. The unstructured grid

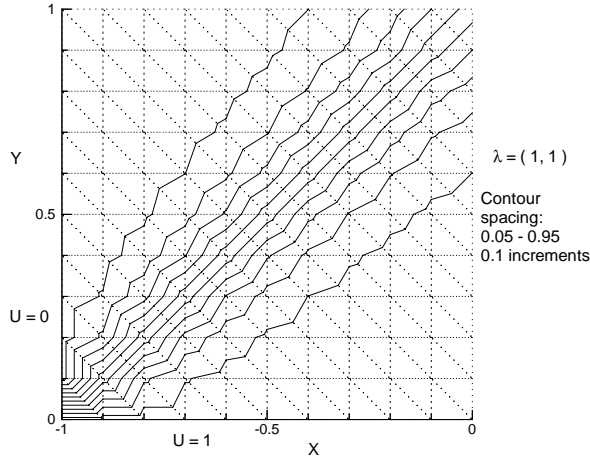


Fig. 5 Second-order fluctuation splitting, uniform advection.

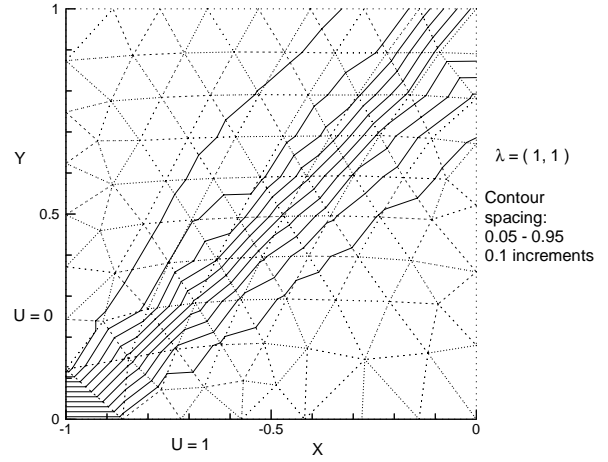


Fig. 8 Fluctuation splitting on unstructured mesh.

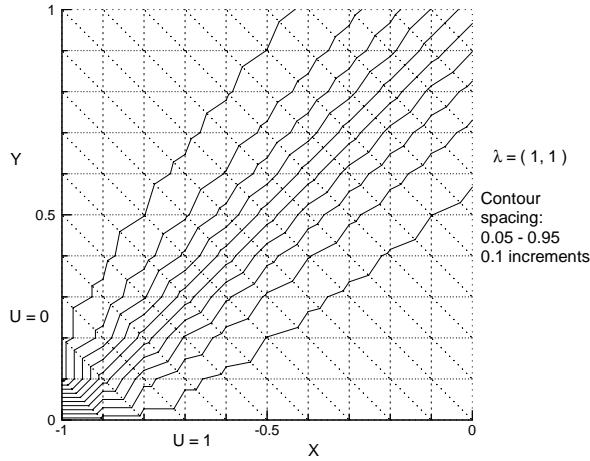


Fig. 6 Second-order finite volume, uniform advection.

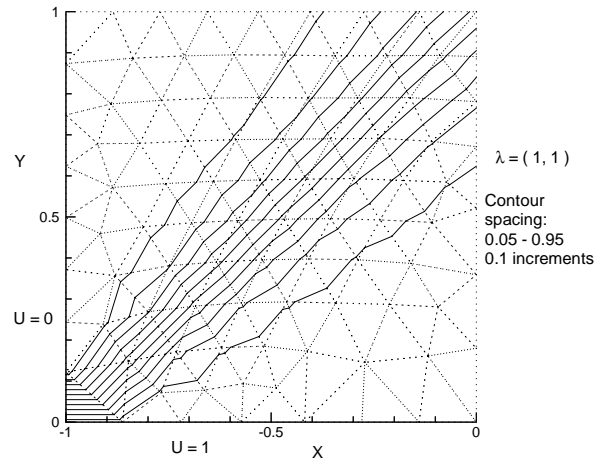


Fig. 9 Finite volume on unstructured mesh.

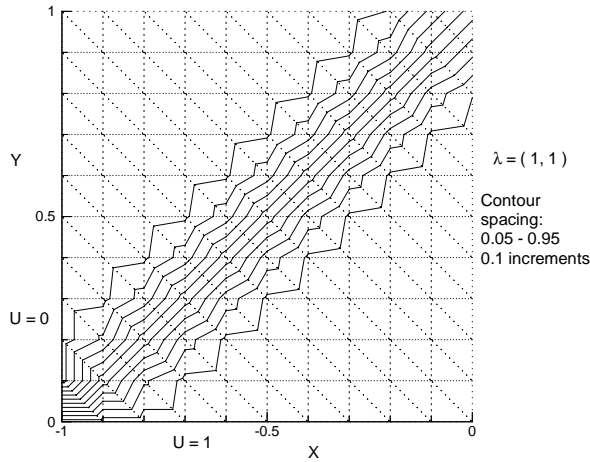


Fig. 7 Second-order fluctuation splitting with compressive limiter.

in this case was generated using VGRID.^{16,17} The FS solution exhibits less dissipation, but is not as smooth as the FV solution. While the FS scheme preserves contact discontinuities over larger spatial ranges than the FV scheme, FS does not appear to degenerate gracefully with regard to extreme coarsening of the unstructured mesh for this test case. This behavior could have negative implications for applications employing multigrid convergence acceleration.

Circular Advection

Circular advection is achieved by setting $\vec{\lambda} = (y, -x)$. A decaying sine-wave input profile is used,

$$u(x, 0) = (e^x \sin \pi x)^2$$

Results for the two schemes, using the Minmod limiter, are presented on the worse-case cut-cartesian mesh in Figs. 10 and 11. Again, the FS results are considerably less diffusive than the dimensionally-split FV solution.

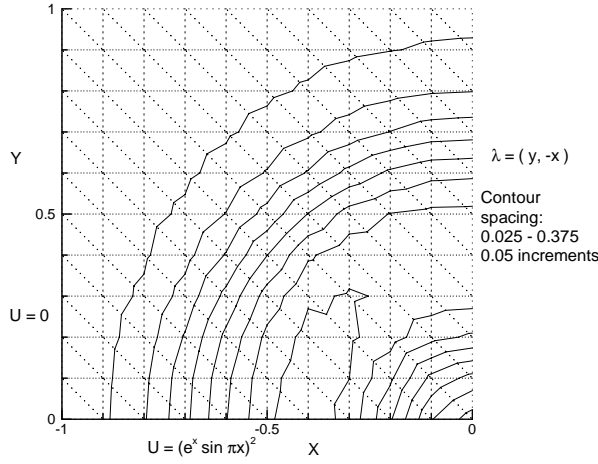


Fig. 10 Fluctuation splitting, circular advection.

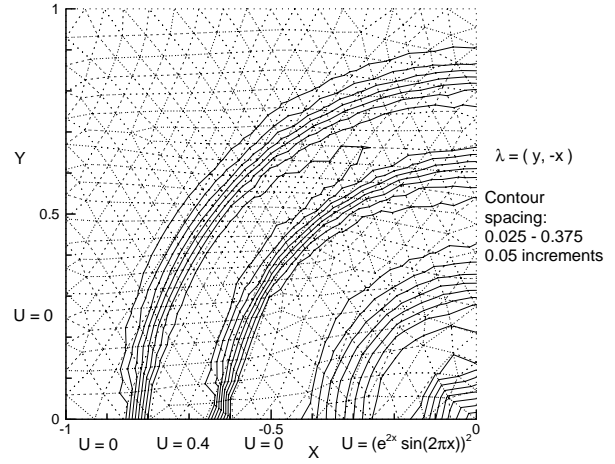


Fig. 12 Fluctuation splitting on unstructured mesh, circular advection.

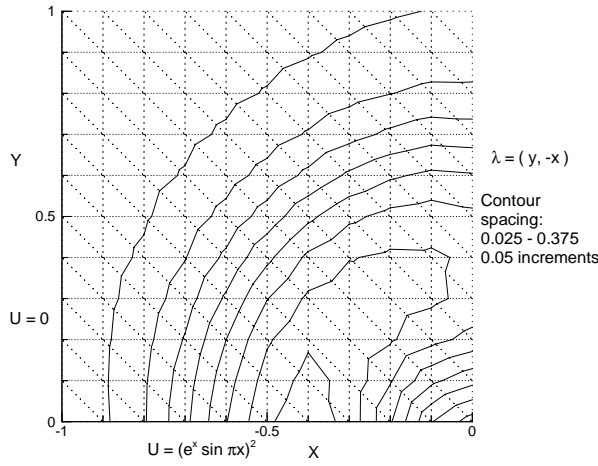


Fig. 11 Finite volume, circular advection.

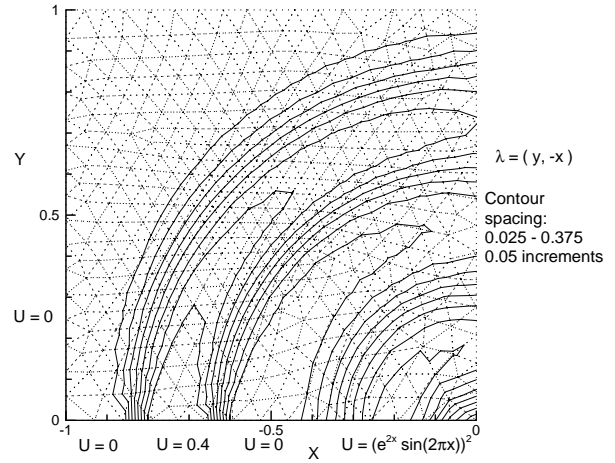


Fig. 13 Finite volume on unstructured mesh, circular advection.

The circular-advection problem is also applied on an unstructured mesh. The input profile for this case consists of both a top-hat function and a decaying sine wave, allowing comparisons between the schemes for both sharp discontinuities and smooth gradients. The input profile is,

$$u(x, 0) = \begin{cases} (e^{2x} \sin(2\pi x))^2 & -0.5 \leq x < 0 \\ 0 & -0.6 \leq x < -0.5 \\ 0.4 & -0.8 \leq x < -0.6 \\ 0 & -1 \leq x < -0.8 \end{cases}$$

Results for this case are displayed in Fig. 12 for FS and Fig. 13 for FV, both using the Minmod limiter. FS performs significantly better at preserving the top-hat distribution. FS also does a better job of maintaining the minimum and maximum values of the sine distribution, though both schemes do well on the smooth gradient portion of the sine wave.

Non-linear Advection

The non-linear advection equation is obtained from Eqn. 1 by setting $\vec{F} = (\frac{u^2}{2}, u)$ with $\nu = 0$. In non-conservative form the equation is written,

$$u_t + uu_x + u_y = 0$$

A coalescing shock problem is considered, with an anti-symmetric input profile,

$$u(-1, y) = u(0, y) = 0$$

$$u(x, 0) = -2x - 1 \text{ on } x = (-1, 0)$$

The exact solution to this problem contains symmetric expansion fans on the sides and a compression fan at the inflow that coalesces into a vertical shock at $(x, y) = (-\frac{1}{2}, \frac{1}{2})$.

The first mesh is cut-cartesian containing 26×26 nodes. The FS and FV solutions, both using the Minmod limiter, are presented in Figs. 14 and 15. Both

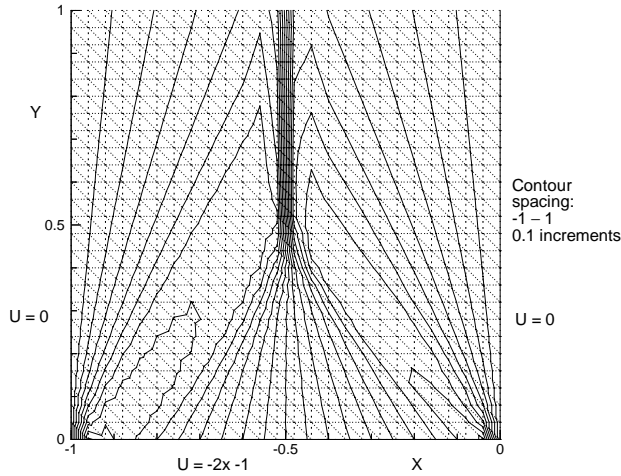


Fig. 14 Fluctuation splitting, Burgers equation.

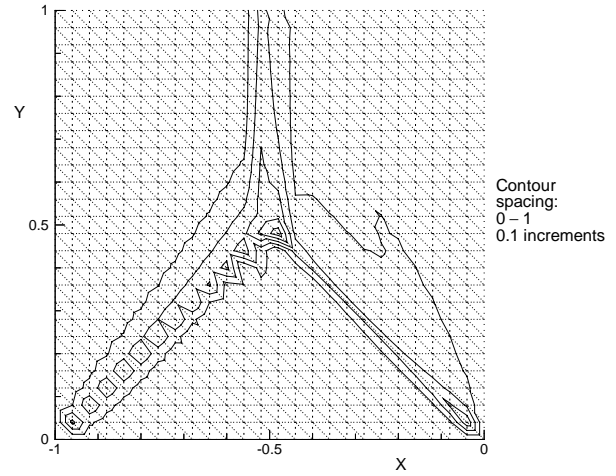


Fig. 16 Fluctuation splitting, Burgers equation, absolute error.

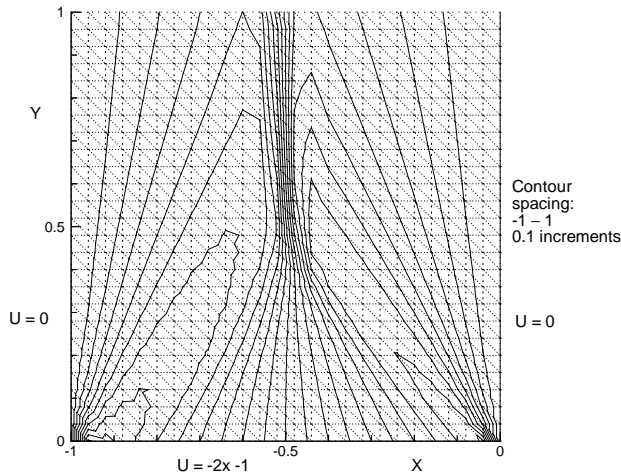


Fig. 15 Finite volume, Burgers equation.

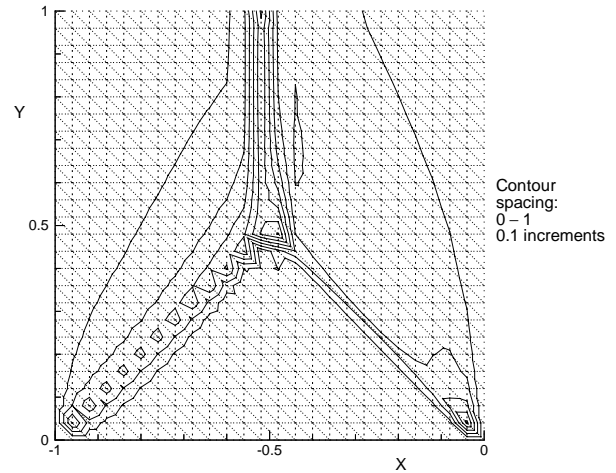


Fig. 17 Finite volume, Burgers equation, absolute error.

algorithms exhibit the same grid dependence on the amount of artificial dissipation as seen before, with the left-half solutions having more diffusion than the right halves, due to the grid orientation. Both methods perform the same in the compression-fan region, coalescing into a shock to within the accuracy of the input-profile discretization.

The shock is more sharply defined by FS than by FV. Fig. 14 has the correct shock speed, with nearly the entire gradient captured in one cell thickness. In contrast, Fig. 15 shows a slightly incorrect shock speed when using FV, as the shock progresses to the left beyond the coalescence point, even though the discretization is conservative. The incorrect shock speed results from a non-symmetric distribution of the dependent variable to the left and right of the shock, caused by the excessive artificial diffusion generated on the grid-misaligned (left-hand) side.

Contours of the absolute value of the error are presented in Figs. 16 and 17. Errors from both computed

solutions show a lack of symmetry, again reflecting the grid dependence of the artificial diffusion terms. The error levels from FS are less than from FV. The shock curvature in the FV solution at the coalescing point is clearly visible in Fig. 17, resulting in significant downstream errors in the shock location as compared with the FS errors.

This problem is repeated on a 25×25 mesh with symmetric diagonal cuts, favorably aligned with the advection directions. The FS and FV solutions, Figs. 18 and 19, are in good agreement. Plots of the absolute error contours, Figs. 20 and 21, show FS to be a little more accurate than FV for this case.

The final mesh for this case is a truly unstructured triangulation containing 847 nodes and 1617 cells. The nodes are clustered to the outflow boundary, with a bias towards the left-hand side. The FS solution is presented in Fig. 22, showing very accurate and crisp shock resolution and good symmetry in the solution

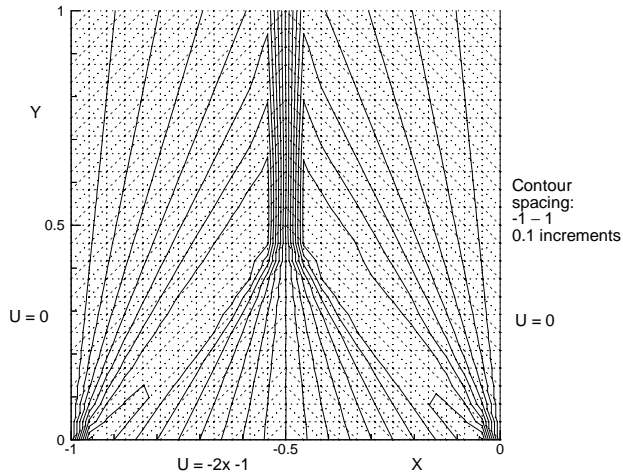


Fig. 18 Fluctuation splitting, Burgers equation, symmetric mesh.

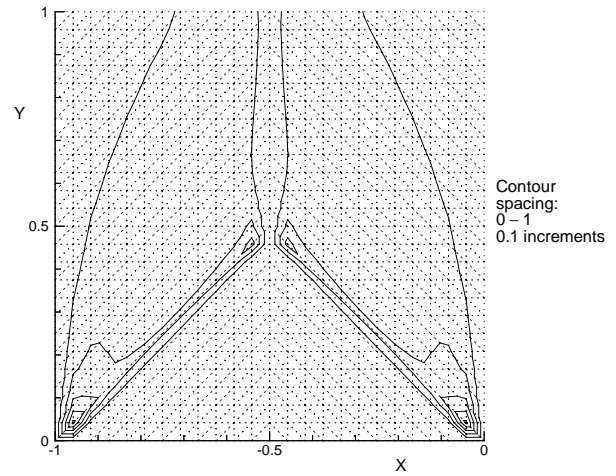


Fig. 21 Finite volume, Burgers equation, absolute error.

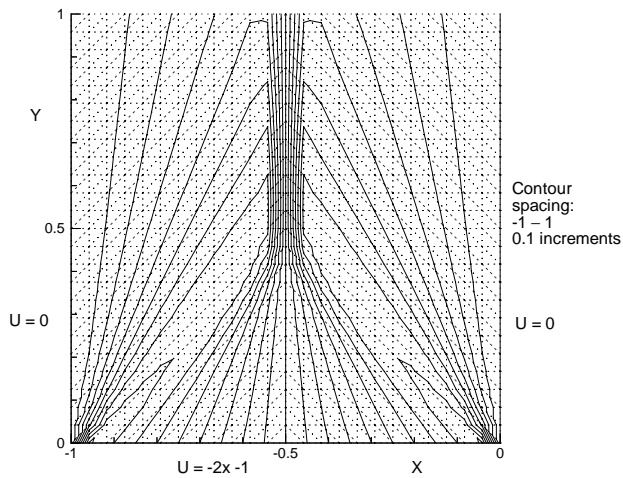


Fig. 19 Finite volume, Burgers equation, symmetric mesh.

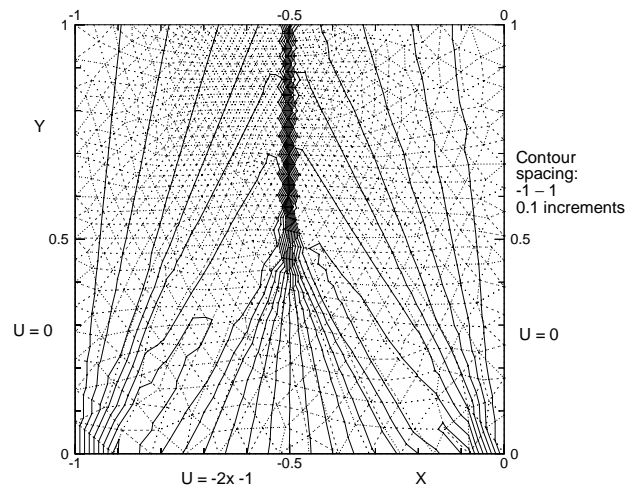


Fig. 22 Fluctuation splitting, Burgers equation, unstructured mesh.

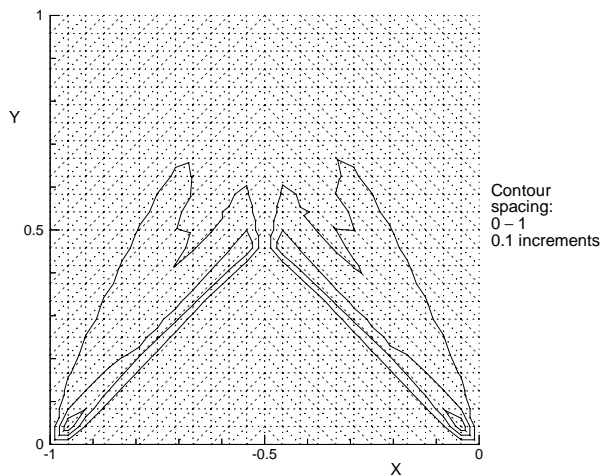


Fig. 20 Fluctuation splitting, Burgers equation, absolute error.

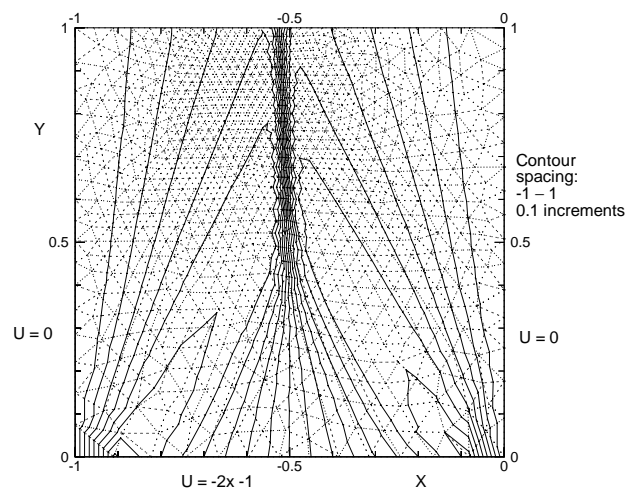


Fig. 23 Finite volume, Burgers equation, unstructured mesh.

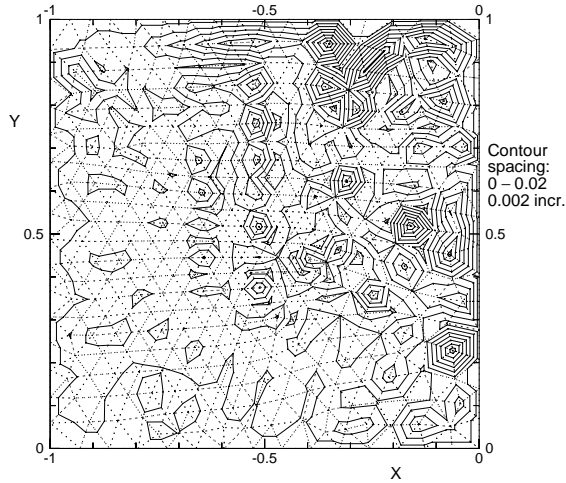


Fig. 24 Pure-diffusion problem error, diffusion terms from Eqn. 8.

contours despite the mesh-clustering bias. In contrast, the FV solution in Fig. 23 has a more-diffuse shock and again an incorrect shock speed, with the outflow shock offset to the left of $x = -\frac{1}{2}$. The FV solution is also somewhat less symmetric than the FS solution.

Linear Diffusion

Choosing $\vec{F} = 0$, the heat-conduction equation is obtained from Eqn. 1,

$$u_t = \nabla \cdot (\nu \nabla u)$$

The test problem, a steady-state boundary value problem on a unit square, is taken from Tomaich.⁴ The Dirichlet boundary values are,

$$u(-1, y) = 0, \quad u(0, y) = \sin(\pi y)$$

$$u(x, 0) = 0, \quad u(x, 1) = -\sin(\pi x)$$

The analytical solution on $x = [-1, 0]$, $y = [0, 1]$ is,

$$u(x, y) = \frac{1}{\sinh \pi} [\sinh(\pi(x+1)) \sin(\pi y) + \sinh(\pi y) \sin(\pi(x+1))]$$

Both diffusion discretizations, Eqns. 8 and 26, are compared on a 438-node unstructured mesh. Figures 24 and 25 plot the absolute value of the error in the converged solutions using Eqns. 8 and 26, respectively.

The finite element treatment is clearly more accurate, and is used to discretize the diffusion terms for both FV and FS in the following section. The average-gradient results in Fig. 24 appear to exhibit a decoupling mode, similar to odd/even decoupling for structured meshes.

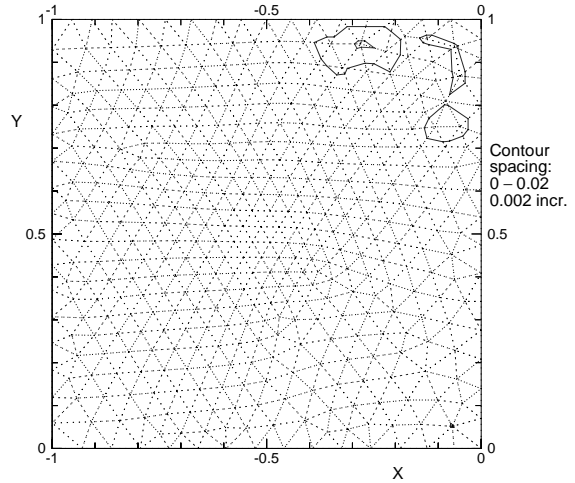


Fig. 25 Pure-diffusion problem error, diffusion terms from Eqn. 26.

Linear Advection-Diffusion

The final test case is a linear advection-diffusion problem of Smith and Hutton.¹⁸ The flux function is $\vec{F} = \vec{\lambda}u$, with,

$$\vec{\lambda} = (2y(1 - x^2), -2x(1 - y^2))$$

The streamlines for this problem, while not truly circular, are similar in orientation to the circular advection problem. The inflow profile is,

$$u(x, 0) = 1 + \tanh(20x + 10)$$

The diffusion coefficient is chosen to be a constant, $\nu = 10^{-3}$. No closed-form solution is known to this problem.

A sequence of five unstructured meshes is considered. The meshes, in order of increasing resolution, are: (A) 134 nodes, (B) 495 nodes, (C) 1928 nodes, (D) 7529 nodes, and (E) 28,915 nodes. The meshes have no preferred clustering or stretching and have nominal node-spacings of 0.1, 0.05, 0.025, 0.0125, and 0.00625, labeled as Meshes A–E, respectively.

L_2 -norms of the artificial and physical dissipations computed using both FS and FV are presented for each mesh in Table 1. Notice that the norm of the artificial dissipation for FS is lower than the norm of the physical dissipation on Meshes D and E. In contrast, the artificial dissipation from FV is still larger than the physical dissipation even on the finest grid. Since the algorithms select only the larger of the physical or artificial dissipation (Eqn. 27), Table 1 suggests FS is grid resolved on Mesh D.

Further evidence of a grid-resolved FS solution is seen in Figs. 26 and 27. The FS solution on Mesh E at the outflow boundary is presented along with the inflow profile and the corresponding pure-advection ($\nu = 0$) FS solution in Fig. 26. The pure-advection

Table 1 L_2 -norms ($\times 10^5$) of artificial and physical viscosities for advection/diffusion problem.

FS			FV	
$\ \bar{\phi}\ _2$	$\ \phi_v\ _2$		$\ \Phi\ _2$	$\ \phi_v\ _2$
(art.)	(phys.)	Mesh	(art.)	(phys.)
1274	215	A	1918	190
597	265	B	640	176
192	161	C	153	107
54	76	D	123	59
13	36	E	45	34

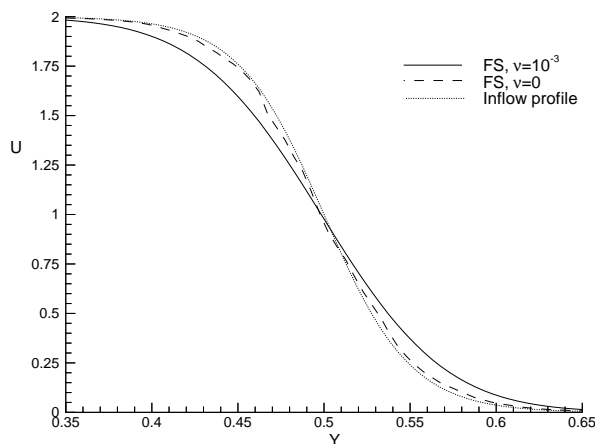


Fig. 26 Fluctuation splitting profiles on finest mesh, advection/diffusion problem.

solution is seen to replicate the inflow profile extremely well, with a clear separation from the diffused, $\nu = 10^{-3}$, solution. Plotting only the FS results with respect to grid refinement, Fig. 27 shows a convergence of the outflow profile by Mesh C for FS.

The accuracy of FS and FV are compared in Fig. 28, where the Mesh-E outflow solutions from FS and FV are plotted along with the Mesh-C FS result. Taking the FS Mesh E solution to be the “truth” solution, it is clear that FS on Mesh C is more accurate in this case than FV is on the finest mesh.

Computational efficiencies of the two algorithms are compared in Fig. 29, where the L_2 -norm of the residual is plotted versus CPU time for the fine-mesh FS and FV solutions, along with the FS convergence history on Mesh D. The Mesh-E FS solution converges in 700 sec on a 195 MHz SGI R10000 CPU. The corresponding FV solution takes 2.7 times longer than FS, due, in part, to the need to reconstruct gradient information at each node with FV for second-order spatial accuracy. However, considering the solution time to reach a given accuracy, it is more reasonable to compare the FS solution time on Mesh D to the finest-mesh

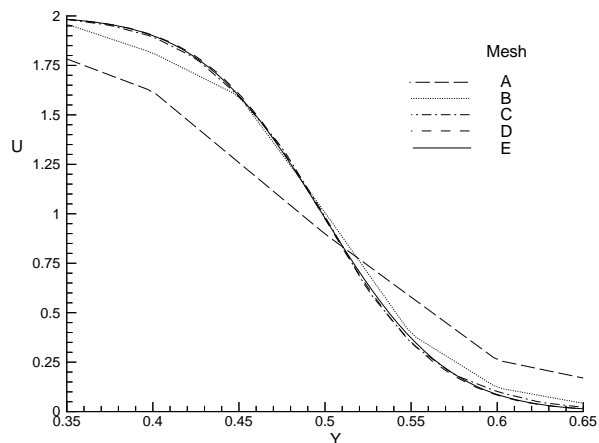


Fig. 27 Fluctuation splitting grid convergence, advection/diffusion problem.

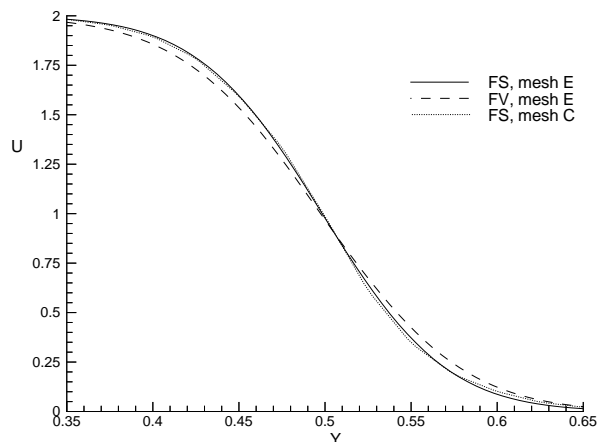


Fig. 28 Fluctuation splitting and finite volume for advection/diffusion problem.

FV solution. The FS Mesh-D solution took only 80 sec, a factor of 23.6 times less than FV on Mesh E, and still shows better accuracy than the fine-mesh FV solution.

An even greater speedup is seen with FS in conjunction with the van Albada limiter, where now the Mesh-B solution over-plots the curve from the finest grid, shown in Fig. 30. The corresponding FV result using the van Albada limiter on Mesh B is included, and clearly falls short of the FS accuracy. The FV case was repeated with the highly-compressive Superbee limiter with little improvement in accuracy. The solution time for FS on Mesh B is three seconds, yielding a speedup factor of 600 over FV.

The final set of results addresses convergence issues while pushing the positivity limits. Figure 31 compares two convergence histories for the second-order FS on Mesh B. The non-converging, though stable, convergence history is the result of using strict positivity arguments to set the timestep (Eqn. 36). The

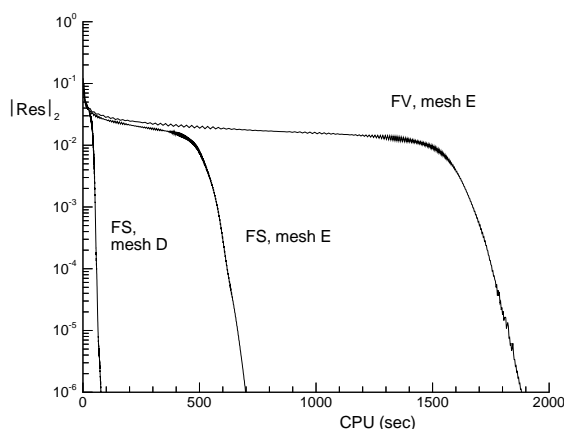


Fig. 29 Convergence histories for advection/diffusion problem.

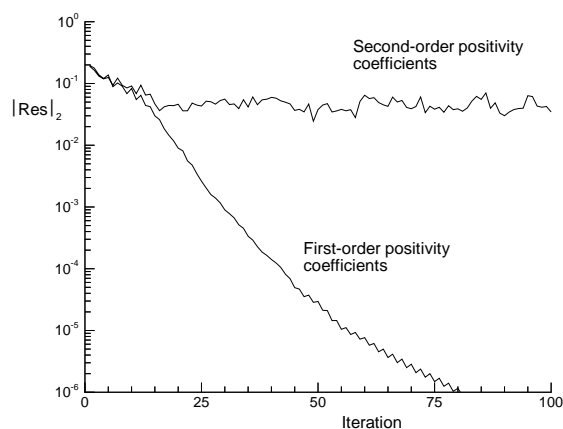


Fig. 31 Convergence rates using first- and second-order positivity coefficients.

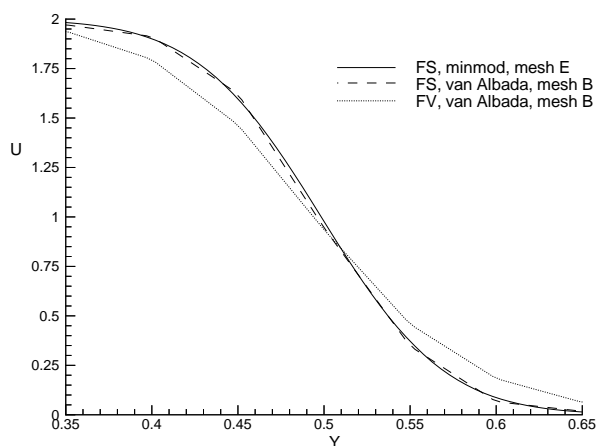


Fig. 30 Advection/diffusion results using van Albada limiter.

resulting solution is bounded and approximately correct but oscillatory—attributed to limiter “ringing”. Full convergence is achieved by using first-order positivity coefficients, which are not dependent on the limiters. The resulting local timesteps will not be as large as true second-order positivity would allow, but appear to be more robust.

Summary of Results

Fluctuation splitting and dimensionally-split finite volume schemes are compared in detail as applied to scalar advection, diffusion, and advection-diffusion problems. The fluctuation splitting scheme is seen to introduce less artificial dissipation while treating advection terms, allowing for more accurate resolution of weakly dissipative advection-diffusion problems. The ability to resolve solutions to these problems on coarser meshes makes the fluctuation splitting scheme the preferred choice over dimensionally-split finite volume.

Linear advection test problems are utilized to investigate the dependence of artificial diffusion production on grid orientation. Both fluctuation splitting and finite volume are shown to exhibit grid dependencies, but with fluctuation splitting producing less artificial dissipation on all grids considered.

A non-linear coalescing shock problem further explores grid dependencies as cases are constructed that result in incorrect shock speeds for finite volume. Fluctuation splitting shows correct shock speeds for all grids and provides tighter shock capturing than finite volume.

An advection-diffusion problem with small physical dissipation (diffusion coefficient of 10^{-3}) is considered where the reduction in artificial dissipation with fluctuation splitting results in a significant accuracy improvement over finite volume. Convergence times are compared, showing a speedup of 2.7 for fluctuation splitting over finite volume on identical grids, using an explicit point Gauss-Seidel relaxation. However, a grid convergence study shows fluctuation splitting has better resolution of the solution on a coarser mesh than finite volume does on the finest mesh, resulting in a speedup of 23.6 for fluctuation splitting over finite volume.

Based upon these significantly reduced solution times for solving model problems, as compared to the current state-of-the-art dimensionally-split finite volume method, fluctuation splitting is considered a worthwhile scheme to pursue for modeling fluid dynamic problems.

References

- ¹Barth, T. J., “Aspects of Unstructured Grids and Finite-Volume Solvers for the Euler and Navier-Stokes Equations,” *Computational Fluid Dynamics*, No. 1994-04 in Lecture Series, von Karman Institute for Fluid Dynamics, 1994.
- ²Mesaros, L. M., *Multi-Dimensional Fluctuation Splitting*

Schemes for the Euler Equations on Unstructured Grids, Ph.D. thesis, University of Michigan, USA, 1995.

³Sidilkover, D. and Roe, P. L., "Unification of Some Advection Schemes in Two Dimensions," Report 95-10, ICASE, Hampton, Feb. 1995.

⁴Tomaich, G. T., *A Genuinely Multi-Dimensional Upwind-ing Algorithm for the Navier-Stokes Equations on Unstructured Grids Using a Compact, Highly-Parallelizable Spatial Discretization*, Ph.D. thesis, University of Michigan, USA, 1995.

⁵Carette, J.-C. and Deconinck, H., "Adaptive Hybrid Remeshing and SUPG/MultiD-Upwind Solver for Compressible High Reynolds Number Flows," AIAA Paper 97-1857, May 1997.

⁶Bathe, K.-J., *Finite Element Procedures in Engineering Analysis*, Prentice-Hall, Inc., Englewood Cliffs, USA, 1982.

⁷Roe, P. L., "Approximate Riemann Solvers, Parameter Vectors, and Difference Schemes," *Journal of Computational Physics*, Vol. 43, October 1981, pp. 357-372.

⁸Anderson, W. K. and Bonhaus, D. L., "An Implicit Upwind Algorithm for Computing Turbulent Flows on Unstructured Grids," *Computers and Fluids*, Vol. 23, No. 1, Jan. 1994, pp. 1-21.

⁹Deconinck, H., Roe, P. L., and Struijs, R., "A Multidimensional Generalization of Roe's Flux Difference Splitter for the Euler Equations," *Computers and Fluids*, Vol. 22, No. 2/3, 1993, pp. 215-222.

¹⁰Sidilkover, D., "A Genuinely Multidimensional Upwind Scheme and Efficient Multigrid Solver for the Compressible Euler Equations," Report 94-84, ICASE, USA, Nov. 1994.

¹¹Chakravarthy, S. R. and Osher, S., "High Resolution Applications of the Osher Upwind Scheme for the Euler Equations," AIAA Paper 83-1943, Jun. 1983.

¹²Bruner, C. W. S. and Walters, R. W., "Parallelization of the Euler Equations on Unstructured Grids," AIAA Paper 97-1894, Jun. 1997.

¹³van Albada, G. D., van Leer, B., and Roberts, W. W., "A Comparative Study of Computational Methods in Cosmic Gas Dynamics," Report 81-24, ICASE, Hampton, Aug. 1981.

¹⁴Hirsch, C., *Numerical Computation of Internal and External Flows—Volume 2: Computational Methods for Inviscid and Viscous Flows*, John Wiley & Sons Ltd., 1990.

¹⁵Spekreijse, S., "Multigrid Solution of Monotone Second-Order Discretization of Hyperbolic Conservation Laws," *Mathematics of Computation*, Vol. 49, 1987, pp. 135-155.

¹⁶Pirzadeh, S., "Three-Dimensional Unstructured Viscous Grids by the Advancing-Layers Method," *AIAA Journal*, Vol. 34, No. 1, Jan. 1996, pp. 43-49.

¹⁷Pirzadeh, S., "Progress Toward a User-Oriented Unstructured Viscous Grid Generator," AIAA Paper 96-0031, Jan. 1996.

¹⁸Smith, R. M. and Hutton, A. G., "The Numerical Treatment of Advection: A Performance Comparison of Current Methods," *Numerical Heat Transfer*, Vol. 5, 1982.